

A tree-based kernel for densities and its applications in clustering DNase-seq profiles

Yuliang Xu¹, Kaixuan Luo², and Li Ma¹

Department of Statistics & Data Science Institute, University of Chicago¹

Department of Human Genetics, University of Chicago²

Abstract

Modeling multiple sampling densities jointly using a hierarchical model allows for borrowing of information across the samples. Such “density random effects” can also serve as kernels in latent variable models to represent exchangeable subgroups or clusters. An important aspect of these kernels is the (functional) covariance they induce, which plays a critical role in identifying the latent subgroups of interest. For example, when applied in mixture models for clustering, the kernel covariance is key to determining what densities are in the same cluster versus those that are not. In particular, we consider the clustering of chromatin accessibility profiles in high-throughput genomic experiments for identifying transcription factor (TF) binding events. Transcription factor (TF) binding typically results in footprint profiles that display certain spatial patterns over genomic locations, which corresponds to a covariance with long-range dependency over the genomic locations. Existing nonparametric hierarchical models on densities impose restrictive assumptions on the covariance and thus cannot accommodate such dependencies. Consequently, clustering using mixture models based on these kernels often produces results that lack biological meaning. We propose a nonparametric density kernel that can accommodate a variety of covariances. We tailor it to reflect the spatial patterns observed in TF footprint profiles from DNase-seq experiments. Our model is based on specifying the splitting probabilities along a dyadic tree over the sample space using a multivariate logit-normal model along with a sparse precision matrix. Bayesian inference for latent variable models using this kernel can proceed with Gibbs sampling using Pólya-Gamma augmentation. We demonstrate how this kernel leads to substantial improvement in clustering accuracy through a variety of simulation scenarios. We apply the enhanced mixture model to DNase-seq data from the ENCODE project, which results in biologically meaningful clusters corresponding to binding events of two common TFs.

Keywords: Bayesian inference; nonparametric models; latent variable models; hierarchical models; tree-based models.

1 Introduction

Many modern biomedical applications require modeling multiple samples each consisting of i.i.d. observations drawn from an unknown distribution. The sampling distributions are often assumed to be exchangeable, which parallels the classical scenario of Gaussian hierarchical models where these sampling densities are assumed to be Gaussian with their means (and sometimes also their variances) drawn from a population distribution. One can adopt this hierarchical modeling idea but allow the sampling distribution, both at the sample level and at the population level to lie in much richer families than Gaussians. Such hierarchical modeling is a popular theme of recent developments in Bayesian nonparametrics, in which the sampling distributions are characterized by a massive (or even infinite) number of parameters and display a variety of distributional features. Some examples ranges from the hierarchical Dirichlet process (Teh et al., 2006), hierarchical Pitman-Yor processes (Teh, 2006; Camerlenghi et al., 2017), to more recent hierarchical normalized completely random measures (Argiento et al., 2020), and hierarchical Pólya tree (Christensen and Ma, 2020). We note, however, that while these models are nonparametric in the sense that they enjoy large support marginally on each individual sampling distribution they model, they all impose very restrictive constraints on the variation among the sampling distributions due to the small number of parameters they devote to characterizing such functional covariance.

Nonparametric hierarchical models are useful beyond the basic exchangeable setup and can be used as modules in more sophisticated models to tackle a variety of data analytical objectives. One common task involves clustering samples of i.i.d. observations based on their respective sampling distributions (Rodriguez et al., 2008). A motivating application comes from DNase-seq experiments (Song and Crawford, 2010), which is a high-throughput genomic assay to measure chromatin accessibility along the genome. It utilizes DNase-I enzyme, an endonuclease, to cut genomic DNA. By sequencing the short reads from DNase-seq experiments, researchers could map genomic regions that are more accessible (open), and

often contain regulatory elements such as promoters and enhancers. TF often regulate gene expression by binding to specific sequence motifs in open chromatin regions. The binding of TFs protects the DNA from DNase-I cleavage, thus often lead to TF specific DNase count profiles, called TF footprints. By clustering these TF footprint profiles, one can infer whether a genomic location is bound or unbound by a transcription factor, providing critical information for understanding gene regulation.

There are several statistical challenges in clustering such count profiles. The count vectors are usually high-dimensional, overdispersed, and exhibit complex correlation structures driven by biological and spatial factors. Nevertheless, samples of the count vectors often show different distributional patterns across different subgroups, and this forms the basis for differentiating clusters. In the example of DNase-seq profile data, the TF binding sites usually have low DNase-seq read counts in the TF motif region and high counts in the two flanking regions, showing a bimodal pattern, since the binding sites are less open to enzyme consumption (see Figure 3). An effective clustering method must distinguish the cross-group difference from within-group heterogeneity while accounting for the dependence structure across different areas in the support.

A variety of methods have been proposed for clustering count vectors. Popular off-the-shelf clustering methods, such as K-means and Partitioning Around Medoids (PAM), directly use the geometric distance between these samples, which does not adequately account for the complex within-cluster covariance. Various mixture models have also been introduced to carry out clustering, and they may adopt either parametric or nonparametric mixture components. In particular, Holmes et al. (2012) adopted a mixture of Dirichlet kernels for each cluster, which assumes that even within a cluster, the counts across the elements in the vector are independent up to a total-sum constraint. Extending the vector to possibly involve an infinite number of elements, the nested Dirichlet Process (NDP) (Rodriguez et al., 2008) also adopts a mixture model of the Dirichlet kernel, but instead assuming all vectors in

the same clusters must have no heterogeneity, i.e., they must share an identical distribution, thereby enforcing the strongest possible dependence: no heterogeneity within each group. Christensen and Ma (2020) and Mao and Ma (2022) considered a mixture model with a finite Pólya tree kernel (Ferguson, 1973; Lavine, 1992; Dennis III, 1991), but the within-cluster correlation is strictly determined by an underlying dyadic tree structure on the genomic locations, without regard to the actual data at hand.

In the domain of DNase-seq profiling, some tailor-made clustering methods utilize additional domain knowledge beyond the count data itself to mitigate the lackings of standard clustering algorithms. These include the site-centric methods, such as early works using k-means (Boyle et al., 2011), mixture model-based and covariate-assisted clustering such as CENTIPEDE (Pique-Regi et al., 2011), and PIQ (protein interaction quantitation) (Sherwood et al., 2014); as well as segmentation-based methods, such as Gusmao et al. (2014) that scans the whole genome into open/closed chromatin and protected footprint states. These methods are less transferable to other domains of count data clustering.

In this paper, we propose a general-purpose mixture model that affords more flexible covariance to capture various types of within-cluster heterogeneity. After introducing the general model, we tailor it to the context of DNase-seq profiling. Building on tree-based kernels in mixture models (Christensen and Ma, 2020; Mao and Ma, 2022), our model allows within-group covariance to deviate from the fixed structure imposed by a dyadic tree based on empirical evidence attained from the data. This adaptivity is achieved through a Bayesian paradigm by first endowing the sampling model (i.e., the likelihood) with more flexible covariance, and placing a prior on the covariance, enabling the model to learn correlation patterns that reflect the observed data *a posteriori*, thereby enhancing the accuracy of the resulting clustering.

We develop an efficient sampling algorithm of the proposed model with R package implementation, and demonstrate its advantages in both simulated and real data. Simulation

studies show that our method outperforms existing clustering approaches under a variety of realistic conditions. We further apply the model to the Encyclopedia of DNA Elements (ENCODE) Consortium (Consortium et al., 2012) DNase-seq data to cluster TF footprints, where it achieves improved accuracy relative to benchmark methods and aligns with the reference biological truth validated by the ChIP data.

The rest of this paper is organized as follows. Section 2 introduces our proposed correlated tree model and its theoretical properties. Section 3 provides details on the sampling algorithm. Section 4 provides numerical evidence of the superior performance of our proposed methods based on simulation studies. Section 5 gives the biological background of the DNase-seq data and the numerical comparison of our method with the competing methods and reference truth. We conclude with a discussion on the potential extensions and limitations in Section 6.

2 A tree-based sampling model for count histograms with flexible covariance

Our proposed sampling model is based on recursive dyadic partitioning of the sample space. At each split, the probability mass is divided between two child nodes, parameterized by the conditional splitting probabilities. We model the conditional splitting probabilities with a prior that accounts for the spatial correlation.

2.1 The dyadic tree specification of probability distributions

We begin with a brief introduction to a tree-based parameterization of a probability distribution. This parameterization has been used in both Bayesian (Ferguson, 1973; Lavine, 1992) and non-Bayesian (Dennis III, 1991) literature to model probability distributions. We will later use this parameterization to construct a new model.

Visualized in Figure 1a, we consider a constructive process in which a probability distribution P can be described through sequential splitting of the unit mass along a dyadic partition tree on the sample space \mathfrak{X} . Let $\mathcal{T}_0 = \{\mathfrak{X}\}$, $\mathcal{T}_1 = \{A_0, A_1\}$, $\mathcal{T}_2 = \{A_{00}, \dots, A_{11}\}$, and so on. Here, we adopt the binary notations in Chapter 3 Section 3.5 in Ghosal and Van der Vaart (2017). Let l be the layer index, \mathcal{T}_l is the l -th layer partition consisting of 2^l nodes. Each node in \mathcal{T}_l is indexed by a string $\epsilon = \epsilon_1 \dots \epsilon_l$, a length l sequence of 0s and 1s, indicating whether it is a left ($\epsilon_l = 0$) or right ($\epsilon_l = 1$) child in each step of the tree split. Let $\mathcal{E} = \{0, 1\}$, \mathcal{E}^l the collection of strings $\epsilon_1 \dots \epsilon_l$ of length l , which is the index set for \mathcal{T}_l , and $\mathcal{E}^* = \bigcup_{l=0}^{\infty} \mathcal{E}^l$. In each split, $A_\epsilon = A_{\epsilon 0} \cup A_{\epsilon 1}$ and $A_{\epsilon 0} \cap A_{\epsilon 1} = \emptyset$, and a probability measure P would satisfy $P(A_\epsilon) = P(A_{\epsilon 0}) + P(A_{\epsilon 1})$. The probability mass splits according to the conditional probabilities $V_{\epsilon 0} = P(A_{\epsilon 0} | A_\epsilon)$, and $V_{\epsilon 1} = P(A_{\epsilon 1} | A_\epsilon) = 1 - V_{\epsilon 0}$. The probability mass on any node $\epsilon = \epsilon_1 \dots \epsilon_l \in \mathcal{E}^l$ in this dyadic tree can be recovered by $P(A_{\epsilon_1 \dots \epsilon_l}) = \prod_{j=1}^l V_{\epsilon_1 \dots \epsilon_j}$. Figure 2a provides the visualization of this dyadic partitioning process in a numeric example for two different distributions supported on $[0, 1]$. The top row is one sample drawn from a mixture of two beta distributions with different modes, and the bottom row is another sample drawn from a distribution with one mode.

Figure 2a illustrates the recursive partitioning process. At each level l , the probability distribution P is approximated by a multinomial probability vector of length 2^l . If a sample X_1^P, \dots, X_n^P is drawn from an unknown distribution P , we can partition the sample space \mathfrak{X} by the aforementioned way and count how many X_i^P fall into each set A_ϵ , denoting $n_p(A_\epsilon) = \sum_{i=1}^n I(X_i^P \in A_\epsilon)$. The empirical conditional splitting probability is $\hat{V}_{\epsilon 0} = \frac{n_p(A_{\epsilon 0})}{n_p(A_\epsilon)}$.

2.2 The hierarchical tree model with sparse covariance structure

Let $X_{[m_i]}^i = \{X_1^i, \dots, X_{m_i}^i\}$ be the i -th sample with m_i independent draws from an underlying distribution Q_i . Within each subgroup, the individual densities Q_i are assumed to independently follow the same underlying sampling distribution, in our case, the corre-

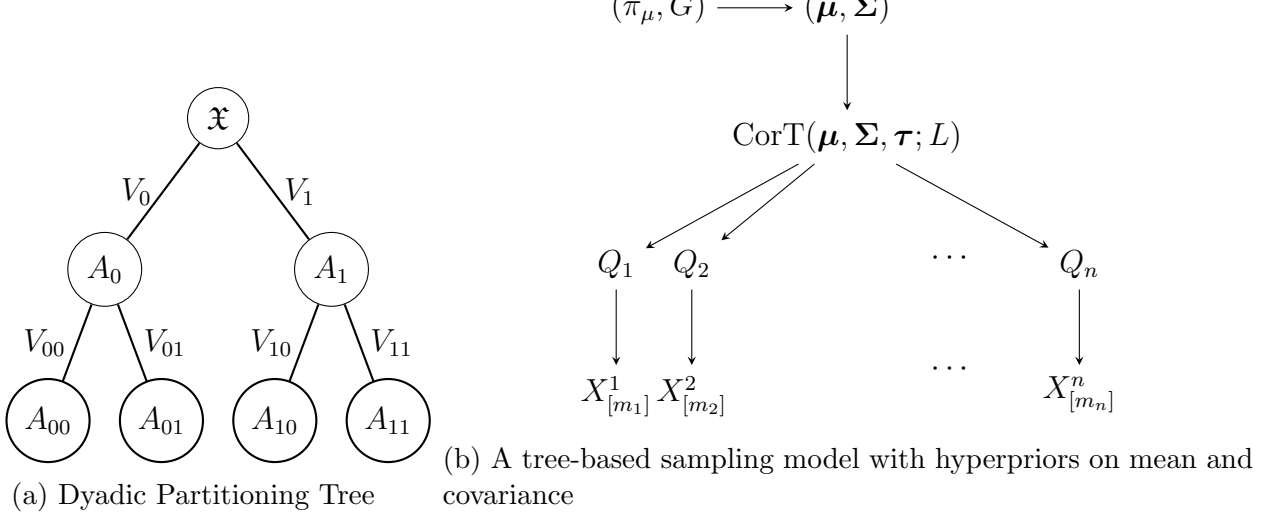


Figure 1: Graphical Illustration of Cor-tree

lated tree distribution. In the observed count data, we only have count vectors of $\mathbf{X}_i = (X_i(B_1), \dots, X_i(B_p))$ where B_1, \dots, B_p are the histogram partition bins, and $X_i(B_j) = \sum_{k=1}^{m_i} I(X_i^k \in B_j)$. With n independent samples, the observed count matrix is $\mathbf{X} = (\mathbf{X}_1, \dots, \mathbf{X}_n)^T$, $\mathbf{X} \in \mathbb{R}^{n \times p}$. In practice, B_1, \dots, B_p are not necessarily the same as the tree leaf nodes, since we use the dyadic partition, and p might not be exactly 2^l , in which case we usually choose the number of layers l so that 2^l is larger than p . In this work, to incorporate the spatial structure, we propose a hierarchical tree model with a sparse covariance structure. The hierarchical structure is illustrated in Figure 1b, where Q_i is represented by a tree-structured density learner defined below.

Definition 1 formally defines a nonparametric tree model indexed by the transformed splitting probabilities $\psi = \{\psi_\epsilon, \epsilon \in \mathcal{E}^*\}$. Let $\text{logit}(p) := \log(\frac{p}{1-p})$, and $\text{logit}^{-1}(\psi) = 1/(1 + \exp^{-\psi})$.

Definition 1 (Dyadic Tree with parameter ψ). *Given the sample space \mathfrak{X} and a dyadic partition sequence $\{\mathcal{T}_l\}_{l=0}^\infty$, let $\psi_\epsilon = \text{logit}(V_\epsilon)$. Then we say that X follows a Dyadic Tree distribution with parameter ψ and write $X \sim \text{Tree}(\psi)$ if starting from $\epsilon = \emptyset$, $X(A_{\epsilon 0}) \sim \text{Bin}(X(A_\epsilon), \text{logit}^{-1}(\psi_{\epsilon 0}))$ for all ϵ .*

Our main strategy for incorporating spatial correlation is to transform the conditional splitting probability $V_{\epsilon 0}$ to the real line by the logit transform $\psi_\epsilon = \text{logit}(V_\epsilon)$ (Jara and Hanson, 2011), and assign a multivariate normal distribution on the vectorized ψ_ϵ across different locations A_ϵ . The logit transform in Definition 1 enables us to define a tree model with a covariance structure. Let $I_c \subset \mathcal{E}^*$ be the index set of all correlated splitting probabilities. For computational convenience, we let the first L layers of splitting probabilities be correlated. Because $V_{\epsilon 1} = 1 - V_{\epsilon 0}$, only including the left splitting probabilities in I_c is sufficient. Hence $|I_c| = \sum_{l=1}^L 2^{l-1} = 2^L - 1$.

Definition 2 (Fixed-layer Correlated Tree). *ψ is said to have a Fixed-layer Correlated Tree distribution if for a fixed integer $L > 0$, $\psi_L = \{\psi_\epsilon : \epsilon \in I_c\} \in \mathbb{R}^{2^L - 1}$,*

$$\begin{aligned} \psi_L &\sim N(\boldsymbol{\mu}, \boldsymbol{\Sigma}), \\ \psi_\epsilon &\stackrel{\text{ind}}{\sim} N(\mu_\epsilon, \sigma_\epsilon^2), \quad \epsilon \in \mathcal{E}^* \setminus I_c \end{aligned} \tag{1}$$

Let $\boldsymbol{\tau} = \{\mu_\epsilon, \sigma_\epsilon^2\}_{\epsilon \in \mathcal{E}^* \setminus I_c}$ be the collection of parameters in the independent tail splitting variables. We write $\psi \sim \text{CorT}(\boldsymbol{\mu}, \boldsymbol{\Sigma}, \boldsymbol{\tau}; L)$ to denote the correlated tree prior specified in (1).

This definition applies to both trees of a finite maximal depth or an infinitely deep tree. We assume that beyond level L , the tail probabilities ψ_ϵ are independent for $\epsilon \in \mathcal{E}^* \setminus I_c$, and μ_ϵ and σ_ϵ^2 both decay to 0 as the layer goes deeper, making the tail splitting variable ψ_ϵ shrink to 0 in the deeper tree nodes. We assign hyperpriors $\sigma_\epsilon^2 \sim \text{InvGamma}(c, 1/l_\epsilon)$ where l_ϵ is the layer of ϵ , $l_\epsilon = \lfloor \log_2 \epsilon \rfloor$, c is an adjustable hyperparameter, default at 1. Similarly, $\mu_\epsilon \sim N(0, \sigma_\mu^2)$ where σ_μ^2 is allowed to decay to 0 for deeper layers. In practice, when we only have a finite tree, σ_μ^2 is set to be a small number.

Such a distribution with finite layers of correlated structure, as in Definition 2, can be used to model both finite histograms and absolute continuous distributions with respect to a base measure λ such as the Lebesgue measure on $\mathfrak{X} = [0, 1]$. In the latter case, it has a

large support that includes all absolutely continuous measures with respect to λ . This allows the models to be applied to continuous sampling distributions as well as finite histograms. While in principle, all real data are discretized at some level (e.g., up to the precision of the measurements or recording), it is helpful to have a sampling distribution supported on density functions that can accommodate long-range dependency such as those induced to symmetry.

Proposition 1. *If P is a random measure with transformed splitting variables $\{\psi_\epsilon, \epsilon \in \mathcal{E}^*\}$ that follow Definition 2, and assume that for the tail splitting variables, $|\mu_\epsilon| \leq \delta_l$ and $\sigma_\epsilon^2 \leq \gamma_l$ for any $\epsilon \in \mathcal{E}^l$ where $l > L$, such that $\sum_l (\delta_l + \gamma_l) < \infty$, then almost all realizations of P are absolutely continuous with respect to λ . In addition, the total variational support of P consists of all probability measures that are absolutely continuous with respect to λ .*

Proof (see details in Supplementary Section S1) of this Proposition directly follows by checking the conditions of Theorem 3.16 and Theorem 3.19 in Ghosal and Van der Vaart (2017). The absolute continuity result in Proposition 1 guarantees that realizations of such random measures can form a density. If the splitting variables divide the mass unevenly (i.e., μ_ϵ is away from 0), the resulting realizations may concentrate around some points rather than forming a density. Proposition 1 also ensures that our prior has full support over the space of probability measures that are absolutely continuous w.r.t. the base measure λ . Both of the results are properties of a tail-free process. A tail-free process is defined as $\{V_{\epsilon 0} : \epsilon \in \mathcal{E}^l\} \perp \{V_{\epsilon 0} : \epsilon \in \mathcal{E}^{l'}\}$ when $l \neq l'$, meaning that the splitting variables across different layers are independent of each other. Our proposed prior in Definition 2 benefits from the good theoretical properties of a tail-free process by having a finite number of layers with correlated splitting variables and an infinite sequence of independent tail splitting variables.

For the mean and covariance of the correlated splitting variables $\psi_L \sim N(\boldsymbol{\mu}, \boldsymbol{\Sigma})$, we let π_μ be $N(0, \sigma_\mu^2 \mathbf{I})$ and assume that G is a sparse covariance. One convenient model that

induces such sparsity in the covariance is the Graphical Horseshoe (GHS) Prior for which there exists simple computational recipes. (See details in Section 3.)

Lastly, for clustering the samples based on their underlying sampling densities, we consider a Dirichlet process mixture (DPM) model with the correlated tree kernel. While one can describe a DPM in several equivalent ways, here we describe it using its stick-breaking representation (Sethuraman, 1994). In the model, Z_i is a latent cluster membership variable for observation i .

Definition 3 (Dirichlet process mixture of correlated trees). *For $i = 1, \dots, n$,*

$$\begin{aligned}
X_i | Z_i = k, \psi_i^k &\sim \text{Tree}(\psi_i^k) \\
\psi_i^k | Z_i = k &\sim \text{CorT}(\boldsymbol{\mu}^k, \boldsymbol{\Sigma}^k, \boldsymbol{\tau}^k; L), \quad k = 1, 2, \dots \\
Z_i | \pi &\sim \text{MultiBern}(\infty, \pi) \\
\pi &\sim \text{GEM}(\alpha)
\end{aligned} \tag{2}$$

where GEM(α) is the Griffiths-Engen-McCloskey stick-breaking model that induces the Dirichlet process with concentration parameter α (Sethuraman, 1994) and MultiBern(∞, π) represents the “infinity multinomial-Bernoulli”, i.e., the discrete distribution with probability π_k on the value k . Specifically, $\pi_k = \beta_k \prod_{b=1}^k (1 - \beta_b)$, $\beta_k \sim \text{Beta}(1, \alpha)$. The superscript k in $\psi^k, \boldsymbol{\mu}^k, \boldsymbol{\Sigma}^k, \boldsymbol{\tau}^k$ indicates cluster-specific parameters. We refer to the hierarchical model (2) as the *Clustering Correlated Tree*.

Now, we have a correlated tree distribution that (i) incorporates the spatial correlation, (ii) is supported on a large class of absolutely continuous distributions, and (iii) can be adopted as a distributional kernel in mixture models for clustering. We next turn to computational strategies for posterior sampling under this model.

3 Computation

We implement the Dirichlet process mixture of correlated trees model using a Gibbs sampler, and the R package Cor-tree is written using RcppArmadillo (Eddelbuettel and Sanderson, 2014) and is available on GitHub (<https://github.com/yuliangxu/Cor-tree>). The posterior sampling of ψ uses the Pólya-Gamma augmentation (Polson et al., 2013). This allows us to have fully conjugate posteriors on ψ . The detailed posterior derivation can be found in the Supplementary Section S2.

In Section 2, the prior on the latent covariance Σ can be any general sparse covariance prior. The sparse covariance prior is a family of distributions that has support on the symmetric and semi-definite matrices and also induces sparsity on the off-diagonal elements. There are also frequentist alternatives of estimating the precision matrix using graphical lasso (Friedman et al., 2008) and the smoothly clipped absolute deviation (SCAD) penalty (Fan and Li, 2001). Such Bayesian priors include the graphical lasso prior (Wang, 2012) and the Graphical Horseshoe (GHS) prior (Li et al., 2019). Here, we choose the most recent state-of-the-art sparse covariance prior, the Graphical Horseshoe prior, which has been shown in Li et al. (2019) to have superior performance in identifying nonzero pairs.

The GHS prior is placed on the precision matrix $\Omega = \Sigma^{-1} \in \mathcal{S}_L$ where \mathcal{S}_L is the space of $L \times L$ positive definite matrices. Let $i, j = 1, \dots, L$, the GHS prior is defined by assigning horseshoe priors on the off-diagonal elements

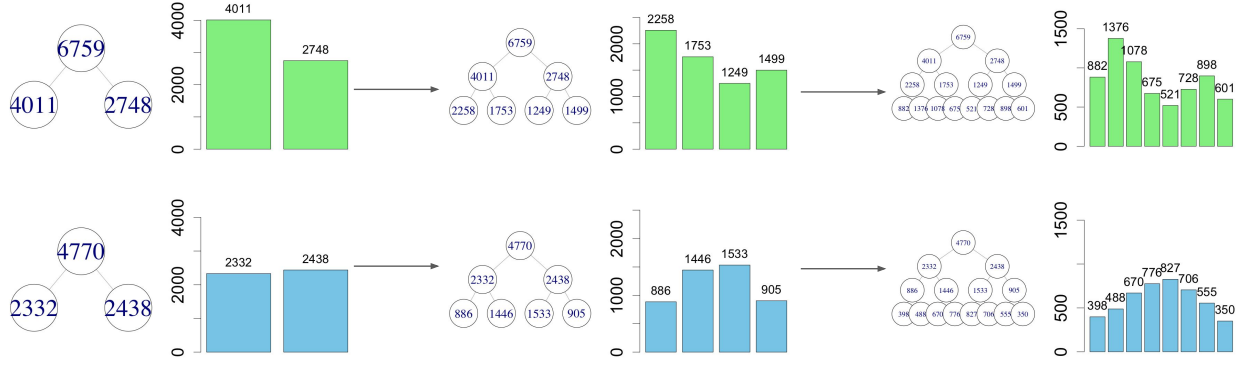
$$\omega_{ii} \propto 1, \quad \omega_{ij: i < j} \sim N(0, \lambda_{ij}^2 \tau^2), \quad \lambda_{ij} \sim C^+(0, 1), \quad \tau \sim C^+(0, 1)$$

where $C^+(0, 1)$ is the half-Cauchy distribution. The prior on Ω can be written as

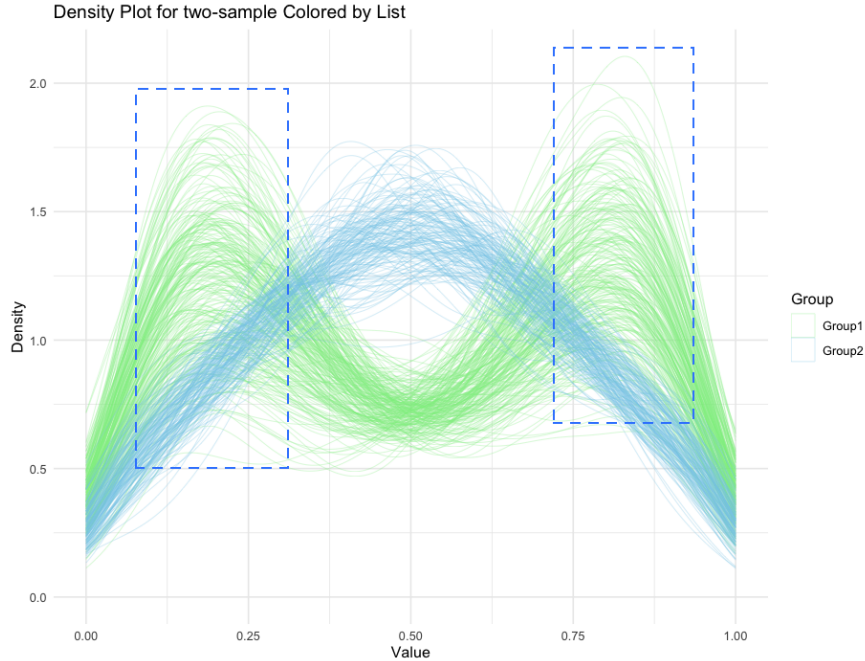
$$p(\Omega | \tau) \propto \prod_{i < j} N(\omega_{ij} | \lambda_{ij}^2, \tau^2) \prod_{i < j} C^+(\lambda_{ij} | 0, 1) 1_{\Omega \in \mathcal{S}_L}.$$

Algorithm 1 in (Li et al., 2019) provides the fully conjugate update of all posteriors. We

provide a C++ implementation for Algorithm 1 in our package based on the MATLAB implementation from the original paper Li et al. (2019).



(a) Recursive partition of the sample space via dyadic tree structure for two different densities.



(b) Density plot for the simulated two groups of samples. The green group with two modes (dashed-line boxed) is designed to mimic the transcription factor (TF) “footprint” pattern.

Figure 2: Illustration of the simulated data example.

4 Simulation Study

To compare our proposed correlated tree method (Cor-tree), we design a simulation study to compare the clustering performance with the following competing methods: (i) K-means (Forgy, 1965); (ii) Partitioning Around Medoids (PAM), implemented in R package `cluster` (Maechler et al., 2024), and (iii) independent tree (Ind-tree), which is essentially the same method as proposed in Christensen and Ma (2020). The only difference between Ind-tree and the HAPT model proposed in (Christensen and Ma, 2020) is that HAPT adopts an adaptive shrinkage on the variance of the splitting probabilities $\text{logit}^{-1}(\psi_\varepsilon)$, whereas Ind-tree sets a fixed decay rate to the variance.

We simulate $X_{[m_j]}^j \stackrel{\text{iid}}{\sim} Q_j$, where Q_j is sampled from a mixture of the following two groups of samples (shown in Figure 2b).

$$\text{Group 1: } Q_j \sim W_j \times \text{Beta}(2, 6) + (1 - W_j) \times \text{Beta}(6, 2), \quad W_j \sim \text{Beta}(10, 10)$$

$$\text{Group 2: } Q_j \sim W_j \times \text{Beta}(1, 1) + (1 - W_j) \times \text{Beta}(3, 3), \quad W_j \sim \text{Beta}(10, 10)$$

Group 1 (green lines in Figure 2b) is a bi-modal distribution with two modes at 1/4 and 3/4 within the support [0, 1]. The bi-modal distribution is designed to mimic the transcription factor (TF) “footprint” pattern in the DNase-Seq data, with a dip in the middle motif region and higher numbers in the flanking regions around the motif (the two modes as dashed lines boxed in Figure 2b). Group 2 (blue lines in Figure 2b) is generated as a unimodal distribution. For each density Q_j , we sample $X_{[m_j]}^j \stackrel{\text{iid}}{\sim} Q_j$ with m_j uniformly sampled from 4×10^3 to 1×10^4 . In addition, each Q_j is a mixture of two beta distributions, with the mixing probability W_j randomly sampled from Beta(10, 10). Hence the variability of Q_j can be visualized in Figure 2b, especially on the green lines. Each line in Figure 2b represents one density Q_j . Some Q_j have a higher left mode than the right mode, and others are the other way around. This is due to the randomness in W_j . We generate a total of n densities

$Q_j, j = 1, \dots, n$, and Q_j is sampled as a mixture from groups 1 and 2, 60% from group 1 and 40% from group 2. After generating $X_{[m_j]}^j$, we compute the histogram of $X_{[m_j]}^j$ with 1000 bins over $[0, 1]$, and use the resulting data as input for clustering algorithms. This gives us $X \in \mathbb{R}^{n \times 1000}$ for each replicated study.

In practice, it is difficult to know *a priori* how many true clusters exist in the data, and the competing methods all require a prespecified number of clusters. Hence, we set the cluster number to be 3 for all methods, although there are only 2 true clusters. To quantify the clustering accuracy, we use the Adjusted Rand Index (ARI), defined in Halkidi et al. (2002) and implemented in the R package `mclust` (Scrucca et al., 2023). ARI can handle label permutation and provides the corrected-for-chance version of the Rand index. Gates and Ahn (2017) shows that ARI is a good criterion for assessing clustering similarity, especially in the case of over-clustering (predicted clusters more than actual clusters). ARI maps the clustering similarity to $[-1, 1]$, with 1 being perfect clustering, 0 being completely random clustering, and -1 being worse than random clustering.

We run three experiments, each with 100 replications. The ind-tree and cor-tree models are implemented using the Gibbs sampler, and the initial value for the membership variable Z_i is set to be the clustering result from PAM. We run 100 MCMC iterations for the burn-in period, and collect the results based on an additional 50 iterations. Both tree models use a 6-layer dyadic tree, and the cor-tree model uses the first 4 layers' splitting variables to be included in the covariance structure, resulting in a covariance matrix of dimension $\mathbb{R}^{31 \times 31}$.

Based on the results in Table 1, among all competing methods, cor-tree achieves the highest mean and median ARI. Both ind-tree and cor-tree models, in some instances, can achieve perfect clustering (ARI=1), although the standard deviation of both tree methods tends to be larger than the distance-based methods (K-means and PAM). This might be due to the random initialization from PAM results.

From Table 1, although rarely, the ind-tree can sometimes produce results where all

Table 1: Clustering results based on 100 replications. Columns meaning from the 3rd column to the last one: mean, median, and standard deviation of ARI over 100 replications, number of times ARI=0 or 1 over 100 replications.

Experiment	Method	Mean ARI	Median ARI	S.D. ARI	# of ARI=0	# of ARI=1
$m = 200$	K-means	0.38	0.38	0.05	0	0
	PAM	0.52	0.52	0.10	0	0
	Ind-tree	0.71	0.83	0.33	5	25
	Cor-tree	0.95	0.98	0.10	0	48
$m = 400$	K-means	0.38	0.38	0.04	0	0
	PAM	0.52	0.50	0.08	0	0
	Ind-tree	0.83	0.99	0.28	1	45
	Cor-tree	0.96	1.00	0.11	0	77
$m = 600$	K-means	0.38	0.38	0.03	0	0
	PAM	0.50	0.49	0.08	0	0
	Ind-tree	0.80	0.97	0.30	4	36
	Cor-tree	0.98	1.00	0.07	0	88

subjects collapse into a single cluster (corresponding to the instance where ARI = 0). After investigating these extreme instances for ind-tree, we find that the ind-tree method is more sensitive to the tree tail shrinkage, in our case, σ_ε in (1), and more specifically c in the $\text{InvGamma}(c, 1/l_\varepsilon)$ prior, whereas cor-tree is much less sensitive to the tail shrinkage. This is because for the ind-tree, due to the independence assumption on ψ_ε , the dispersion in $\psi_{i,\varepsilon}$ is only controlled by the diagonal posterior variance, which is greatly influenced by σ_ε . The variance of $\psi_{i,\varepsilon}$ in cor-tree can be adaptively accounted for through the sparse covariance prior, which allows the marginal variance of $\psi_{i,\varepsilon}$ to be relatively large in the shallow layers of the tree, and adaptively shrinks to 0 for the deep layers.

5 Clustering of TF footprints using DNase-Seq data from ENCODE

5.1 Biological background

TF regulate gene expression in different cell types and conditions. They bind to specific regulatory sequence elements in genomic regions that are accessible. Thus, mapping accessible regions and TF binding sites is critical to understand gene regulation. Over the past decade, researchers have developed genomic assays to profile chromatin accessibility, such as DNase-seq and ATAC-seq. In the DNase sequencing (DNase-seq) data of our interest, a particular enzyme, DNase I, is used to cut DNA at accessible (open) chromatin regions that are not tightly bound by nucleosomes or other proteins. By aligning the sequencing reads from DNase-seq, one can identify regions with high read counts, known as DNase I hypersensitive sites (DHSs), which are often enriched for regulatory elements, including promoters, enhancers, and transcription factor binding sites (TFBS)(Consortium et al., 2012).

Within these DHSs, small regions protected from DNase I cleavage can be observed. These are known as *footprints*. As shown in the heatmap (Figure 3), most of the candidate binding sites have some dips in the middle motif region and higher numbers in the flanking regions around the motif. They reflect sites where DNA-binding proteins, such as transcription factors, shield the DNA from cleavage. By analyzing the pattern of cut frequencies at base-pair resolution, researchers can infer the presence of TFBS. Coupled with known transcription factor motifs, DNase footprinting enables high-throughput localization of TF binding events, providing key insights into gene regulation and chromatin dynamics.

We apply our proposed clustering method to DNase-seq data generated from the ENCODE project, known as the Encyclopedia of DNA Elements (ENCODE) Consortium (Consortium et al., 2012). More specifically, we apply the clustering method for two key transcription factors, REST (RE1-silencing transcription factor) and NRF1 (Nuclear respiratory

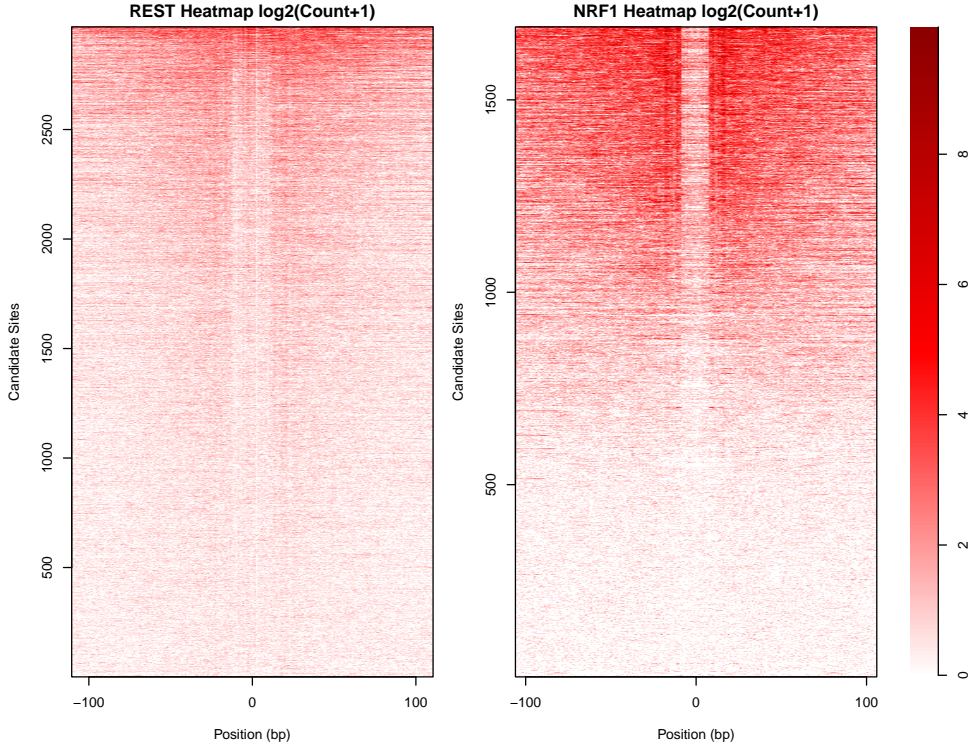


Figure 3: Heatmap of DNase seq data for REST and NRF1 in K562 (cell type). Each row represents one genomic region with motif match in the middle with 100 bp flanking regions on both sides of the motif, and each column represents the log-transformed ($\log_2(X + 1)$) count of DNase-seq reads in the corresponding genomic location. The rows are ordered by the row sum in decreasing order.

factor 1), in the K562 human erythroleukemia cell line. NRF1 maintains cellular energy metabolism and mitochondrial function. REST is a repressor of neuronal gene expression in non-neuronal cells and modulates neurodevelopment.

In addition to the DNase-seq count data, we also have external information to provide initial values and validate the clustering results. The Position Weight Matrix (PWM) is a simple metric widely used to represent the sequence motif of a TF. We use PWMs learned from earlier studies in the JASPAR database (Rauluseviciute et al., 2024) and scan the genomic DNA sequences for locations that show strong matches to the PWM (motif matches, or candidate binding sites). Higher PWM score suggests stronger DNA sequence preference for that TF. PWM scores represents the DNA sequence preference, yet TF binding is also highly influenced by the cellular chromatin environment. So earlier literature often uses

PWM scores as a prior for TF binding. In our analysis, we use the PWM scores as an exclusion criterion in data preprocessing, and use the discretized PWM scores as the initial values for the clustering membership variable Z for the REST data.

Another challenge in unsupervised tasks such as clustering is validation of the results. In the current application, we can use the external data from ChIP-seq (Chromatin ImmunoPrecipitation followed by sequencing). Different from DNase-seq, ChIP-seq uses a TF-specific antibody to target one specific TF at a time (Park, 2009), and has been widely used as a proxy to the *ground truth* of TF binding events. Hence ChIP-seq data is TF-specific, unlike the DNase footprinting, which may be biased due to issues such as transient binding of TFs with shorter residency time, or digestion bias from DNaseI enzyme. We downloaded the ChIP-seq data from the ENCODE portal. We obtain the ChIP-seq read counts at motif match locations normalized by sequencing library size. We also obtain the binary ChIP labels for those motif match locations using the ChIP-seq peaks, and the binary label is 1 if the peaks overlap with the motif match locations. Note that the ChIP count data and binary label data are both based on ChIP-seq, an entirely different genomic technology than DNase-seq, so it is only used as a reference for validation and to compare the clustering results of our method and other competing methods.

5.2 Data Analysis

We scan the human genome with REST and NRF1 motifs using FIMO (a software tool for scanning DNA sequences, Grant et al. (2011)), select motif matches with FIMO p-value $< 1e-5$ and PWM scores ≥ 13 , and take 100 bp flanking regions on both sides of the motif matches as the candidate regions of our analysis. We then combine the DNase counts on both strands, and restrict to candidate regions with at least 100 DNase counts for the REST data, and 50 counts for the NRF1 data.

For REST data, after preprocessing, there are $p = 220$ base pairs (columns) and $n = 2968$

candidate binding sites (rows). The total count per row ranges from 100 to 9399. For the NRF1 data, we focus on the candidate sites on chromosome 1. The count matrix for NRF1 has $n = 1689$ candidate sites and $p = 211$ columns; the row sums range from 50 to 9711.

Note that the count per sample in the real data can be much less than our simulation data where the row sums range from 4×10^3 to 10^4 . Because the cor-tree method builds a mixture model with each component being a nonparametric tree with a covariance structure, it is prone to mode collapsing without a proper initial value. Supplementary Section S3 provides additional simulation results with PAM initial values, where we show that even in the low-count setting, cor-tree can achieve high clustering accuracy as long as it can identify more than one cluster.

In addition to k-means and PAM to be compared in the real data analysis, we also include a state-of-the-art method tailored for DNase-seq data called CENTIPEDE (Pique-Regi et al., 2011), which uses the continuous PWM score as a site-specific covariate. CENTIPEDE uses a simple mixture of two multinomial components as shown in (3) which only clusters sites into 0-1 groups and requires additional site-specific information Y_i .

$$\mathbf{X}_i \in \mathbb{R}^p, \mathbf{X}_i \sim \pi_i \text{Multinomial}(n_i, \boldsymbol{\theta}_1) + (1 - \pi_i) \text{Multinomial}(n_i, \boldsymbol{\theta}_0). \quad \text{logit}(\pi_i) = Y_i^T \boldsymbol{\beta} \quad (3)$$

Here, Y_i is a 2-dimensional vector, $(1, \text{PWM_score}_i)$ to include the intercept term. The unbound sites are simply assumed to be uniformly distributed in CENTIPEDE, which may fail to capture the spatial bias induced by the DNase I enzyme.

Because we use the stick-breaking prior for the mixing weights in (2), theoretically, we can just set a large number of clusters for Cor-tree to learn, and it will naturally collapse to fewer subgroups with group-specific first and second moment structures. For the real data analysis, we first set 5 clusters for Cor-tree to learn potential subgroup structures. Then we set 2 clusters for k-means, PAM, and CENTIPEDE, and compare the clustering results with Cor-tree. We only report clusters with at least 10 observations for all methods.

Supplementary Section S4 provides additional results when k-means and PAM are set to find at most 5 clusters, and sensitivity analysis for Cor-tree when we vary the total number of clusters and other hyperparameters.

5.2.1 REST result

For Cor-tree, the tree structure is set to have 9 layers to have at least one node to represent a single column in the dyadic partition. This dyadic partition leads to many 0s in deeper layers of the tree when the partition ends early, before reaching the pre-set leaf layer. We set the first 4 layers of the splitting probabilities to be included in the sparse covariance structure, leading to a 15×15 covariance matrix for each cluster. To check the model convergence, we only need to check the convergence of mixing weights π in (2) for the clustering purpose. We choose not to use the log-likelihood convergence because the log-likelihood depends on all the splitting variables, which may continue to improve as the transformed splitting variables grow to positive or negative extremes, especially in the deeper nodes. Convergence of the mixing weights can be very fast and is usually achieved within 20 iterations. We run 20 iterations as the burn-in period and collect 10 iterations of MCMC samples after the burn-in. It is possible to run longer iterations as long as the memory permits, although given the vast amount of parameters, especially in ψ , we do not recommend running much longer after convergence. For example, the total number of elements to trace all ψ is $n_{\text{sample}} \times n_{\text{node}} \times n_{\text{mcmc}}$, and in the REST example of a 9-layer tree, sums up to 1.5×10^7 elements to trace 10 iterations of ψ . In the Supplementary Section S4, we provide the traceplots for all π after burn-in for 30 iterations to show the stable convergence. Additional sensitivity analysis in Supplementary Section S4 with varying number of clusters and other hyperparameters yields similar results as the below-reported main result.

Figure 4 provides the binary clustering performance. The first row is the cluster mean of DNase-seq count within each subgroup. The cluster-mean plots help to check the spatial

pattern across genomic locations for each subgroup. They show a clear bimodal pattern for one subgroup, potentially the group of binding sites, and another subgroup with a flat pattern over the genomic locations, potentially the group of unbound sites. Such a mixture of bimodal and flat distributional patterns is most obvious for the binary ChIP label (reference truth) and the Cor-tree label (our method). When restricted to only 2 clusters, k-means and PAM both find a small ($\sim 10\%$ of total subsample) subgroup with an overall high count, and put the rest in one big subgroup. CENTIPEDE can find a subgroup with an asymmetric bimodal pattern, which could also be a potential binding group.

The second row in Figure 4 is the histogram of the ChIP count data stratified by subgroups. The ChIP count histogram provides a 1-dimensional summary of how likely a candidate site could be a binding site. The subgroups identified by K-means and PAM are nearly indistinguishable in the ChIP count distribution. Both CENTIPEDE and Cor-tree can find a subgroup of potential binding sites that also have high ChIP counts, and the binding subgroups (blue) are well distinguished from the unbound subgroups (red). However, if we compare the right tail of the red groups for CENTIPEDE and Cor-tree, CENTIPEDE tends to classify more sites with high ChIP count into the unbound group, whereas such potential misclassified cases in the right-tail are much lower for Cor-tree. Cor-tree uses the discretized PWM score as the initial value. If we use the binary ChIP label as the reference truth, as shown in Table 2, the ARI of Cor-tree is 0.21, and the ARI of the discretized PWM score is 0.125. In comparison, the ARI for CENTIPEDE is 0.158. This also provides evidence that the posterior mean of the membership variables in Cor-tree after convergence are already reasonably away from the initial values and closer to the reference truth. We provide the 5-cluster results for K-means and PAM in the Supplementary Figure S1.

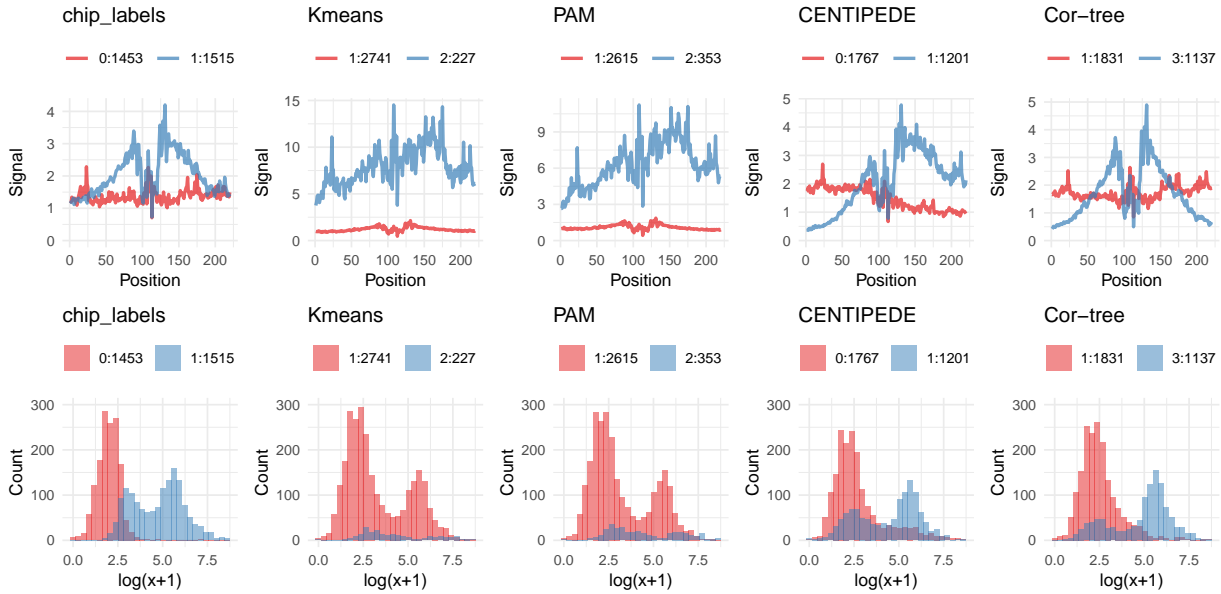


Figure 4: REST data clustering result. K-means, PAM, and CENTIPEDE are set to have 2 clusters. Cor-tree uses 5 clusters but converges to 2 clusters after burn-in. The first column is the reference binary result from ChIP data. The first row is the cluster mean, and the second row is the histograms of the log-transformed ChIP count data. The legend is formatted as *subgroup label:subgroup size*.

5.2.2 NRF1 result

For the NRF1 data, we also set the number of clusters to be 5. Cor-tree uses the 9-layer dyadic tree structure with 3 layers of correlated ψ_i . We collect 20 iterations of MCMC samples after 20 iterations of burn-in. The binary clustering result is shown in Figure 5. For this study, we use the binary k-means result as the initial value for Cor-tree.

Figure 5 shows the cluster result for each method. The NRF1 pattern is quite different from the REST pattern. If we take the ChIP label as the reference truth, the NRF1 data after preprocessing is more unbalanced, where there are more samples in the bound group than the unbound group. From the first row of Figure 5, all methods provide similar cluster mean patterns for the bound and unbound groups. Examining the number of candidate sites in both groups (second row of Figure 5) reveals that only Cor-tree identifies a comparable number of bound sites to the binary ChIP label, whereas the other three methods

consistently underestimate the number of bound sites. Moreover, Cor-tree’s detected bound sites generally exhibit high ChIP counts and its unbound sites low counts, while in the other methods, many unbound sites still show high ChIP counts.

Table 2 shows the ARI comparison with the binary ChIP label for all methods. Cor-tree has the highest similarity with this reference truth (binary ChIP label) in both studies, and the similarity is also much higher than the initial values used by Cor-tree. Note that in NRF1, we no longer use the discretized PWM score as the initial value because this is a poor estimate away from the truth, causing mode collapse for a highly flexible model like Cor-tree, and this can be validated by the lowest ARI of the discretized PWM in Table 2. Instead, we have experimented using K-means, PAM, and CENTIPEDE results as the initial values for Cor-tree, and the result is similar to that reported in Figure 5.

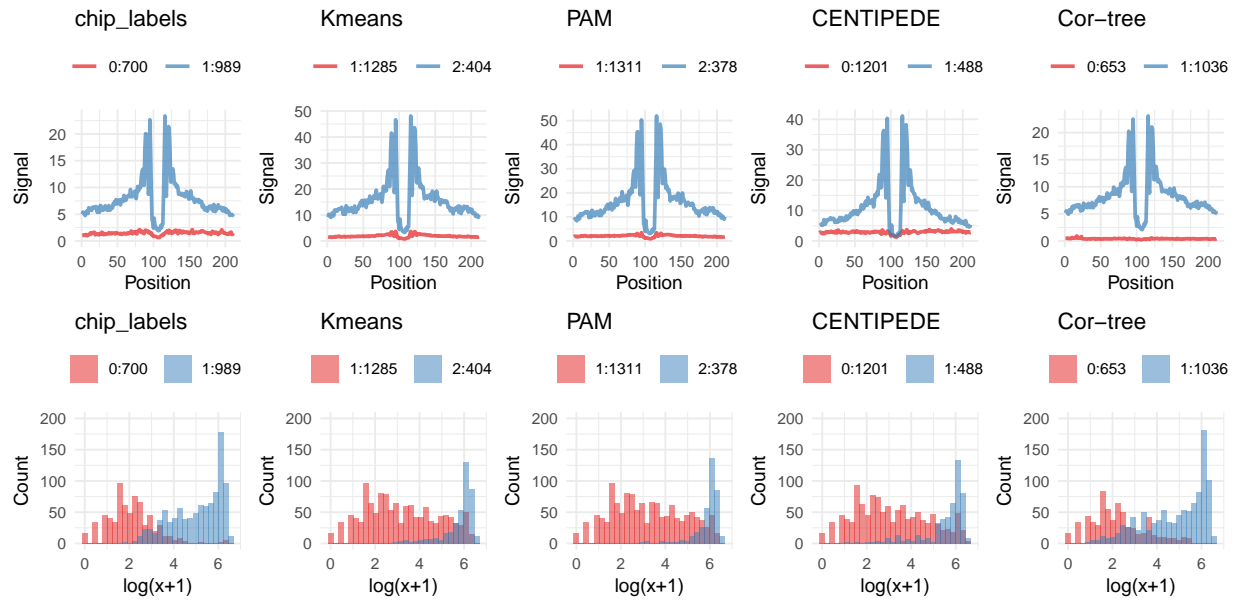


Figure 5: NRF1 data clustering result. K-means, PAM, and CENTIPEDE are set to have 2 clusters. Cor-tree uses 5 clusters but converges to 2 clusters after burn-in. The first column is the reference binary result from ChIP data. The first row is the cluster mean, and the second row is the histograms of the log-transformed ChIP count data. The legend is formatted as *subgroup label:subgroup size*.

Table 2: ARI compared with the binary ChIP label. The first row is for REST, the second row is for NRF1. *PWM_cate* refers to the categorical PWM values, converted from the continuous PWM score into 5 levels, used as the initial value for Cor-tree on the REST data.

	K-means	PAM	CENTIPEDE	PWM_cate	Cor-tree
REST	0.001	0.008	0.158	0.125	0.212
NRF1	0.051	0.048	0.095	0.036	0.279

6 Discussion

We have introduced Cor-tree, a hierarchical tree model enriched with sparse covariance structure in the splitting variables, thereby accounting for long-range dependencies in multi-sample count data. Cor-tree has large prior support in theory, and the covariance matrix is assigned the graphical horseshoe prior to adaptively learn the second moment structure in the MCMC algorithm. Extensive simulations demonstrate that Cor-tree substantially outperforms classical clustering methods such as k-means and PAM, as well as its nonparametric counterpart, the hierarchical tree with independent structure. Furthermore, the learned covariance structure may reveal biologically meaningful correlation pairs among different locations in the support. Combining flexible tree-based density estimation with Bayesian clustering, Cor-tree provides a general solution to finding latent subgroups in high-dimensional count data.

This method can be extended to other settings, such as clustering microbiome count profiles. For microbiome data, one can leverage the phylogenetic tree to incorporate contextual knowledge of the count categories (i.e., the taxa). One could also apply this method to RNA splicing analyses to cluster transcript isoforms. However, there are two main challenges in extending this method to other domains. The first is to find a relatively good initial value for the membership variable. Because Cor-tree is a highly flexible density estimator, inappropriate initial values may lead the MCMC algorithm to be trapped in local modes and fail to converge to the global optimum. The second issue is to have a relatively good ground truth to evaluate the clustering results, such as the ChIP label used in our DNase-seq case

study. This is a common challenge in unsupervised learning tasks such as clustering and requires domain experts to extract meaningful information from the identified subgroups.

Acknowledgements

This research is partly supported by NIGMS grant R01-GM135440.

Data Availability Statement

PWM matrices for REST (MA0138.3) and NRF (MA0506.1) were downloaded from JASPAR 2024 database (Rauluseviciute et al., 2024). TF motif matches were identified using FIMO software (Grant et al., 2011). DNase-seq and ChIP-seq data for REST and NRF in K562 cell line were downloaded from ENCODE portal (Sloan et al. 2016) (<https://www.encodeproject.org/>) with the following identifiers: ENCSR000EMT, ENCSR137ZMQ, ENCSR837EYC. Data were processed using TOP R package (Luo et al., 2022), with more details available at: https://kevinlkx.github.io/footprint_clustering/index.html.

References

Argiento, R., Cremaschi, A., and Vannucci, M. (2020), “Hierarchical normalized completely random measures to cluster grouped data,” *Journal of the American Statistical Association*.

Boyle, A. P., Song, L., Lee, B.-K., London, D., Keefe, D., Birney, E., Iyer, V. R., Crawford, G. E., and Furey, T. S. (2011), “High-resolution genome-wide in vivo footprinting of diverse transcription factors in human cells,” *Genome research*, 21, 456–464.

Camerlenghi, F., Lijoi, A., and Prünster, I. (2017), “Bayesian prediction with multiple-samples information,” *Journal of Multivariate Analysis*, 156, 18–28.

Christensen, J. and Ma, L. (2020), “A Bayesian hierarchical model for related densities by using Pólya trees,” *Journal of the Royal Statistical Society Series B: Statistical Methodology*, 82, 127–153.

Consortium, E. P. et al. (2012), “An integrated encyclopedia of DNA elements in the human genome,” *Nature*, 489, 57.

Dennis III, S. Y. (1991), “On the hyper-Dirichlet type 1 and hyper-Liouville distributions,” *Communications in Statistics-Theory and Methods*, 20, 4069–4081.

Eddelbuettel, D. and Sanderson, C. (2014), “RcppArmadillo: Accelerating R with high-performance C++ linear algebra,” *Computational Statistics and Data Analysis*, 71, 1054–1063.

Fan, J. and Li, R. (2001), “Variable selection via nonconcave penalized likelihood and its oracle properties,” *Journal of the American statistical Association*, 96, 1348–1360.

Ferguson, T. S. (1973), “A Bayesian analysis of some nonparametric problems,” *The annals of statistics*, 209–230.

Forgy, E. W. (1965), “Cluster analysis of multivariate data: efficiency versus interpretability of classifications,” *biometrics*, 21, 768–769.

Friedman, J., Hastie, T., and Tibshirani, R. (2008), “Sparse inverse covariance estimation with the graphical lasso,” *Biostatistics*, 9, 432–441.

Gates, A. J. and Ahn, Y.-Y. (2017), “The impact of random models on clustering similarity,” *Journal of Machine Learning Research*, 18, 1–28.

Ghosal, S. and Van der Vaart, A. W. (2017), *Fundamentals of nonparametric Bayesian inference*, vol. 44, Cambridge University Press.

Grant, C. E., Bailey, T. L., and Noble, W. S. (2011), “FIMO: scanning for occurrences of a given motif,” *Bioinformatics*, 27, 1017–1018.

Gusmao, E. G., Dieterich, C., Zenke, M., and Costa, I. G. (2014), “Detection of active transcription factor binding sites with the combination of DNase hypersensitivity and histone modifications,” *Bioinformatics*, 30, 3143–3151.

Halkidi, M., Batistakis, Y., and Vazirgiannis, M. (2002), “Cluster validity methods: part I,” *ACM Sigmod Record*, 31, 40–45.

Holmes, I., Harris, K., and Quince, C. (2012), “Dirichlet multinomial mixtures: generative models for microbial metagenomics,” *PloS one*, 7, e30126.

Jara, A. and Hanson, T. E. (2011), “A class of mixtures of dependent tail-free processes,” *Biometrika*, 98, 553–566.

Lavine, M. (1992), “Some aspects of Polya tree distributions for statistical modelling,” *The annals of statistics*, 1222–1235.

Li, Y., Craig, B. A., and Bhadra, A. (2019), “The graphical horseshoe estimator for inverse covariance matrices,” *Journal of Computational and Graphical Statistics*, 28, 747–757.

Luo, K., Zhong, J., Safi, A., Hong, L. K., Tewari, A. K., Song, L., Reddy, T. E., Ma, L., Crawford, G. E., and Hartemink, A. J. (2022), “Profiling the quantitative occupancy of myriad transcription factors across conditions by modeling chromatin accessibility data,” *Genome Research*, 32, 1183–1198.

Maechler, M., Rousseeuw, P., Struyf, A., Hubert, M., and Hornik, K. (2024), *cluster: Cluster Analysis Basics and Extensions*, r package version 2.1.8 — For new features, see the 'NEWS' and the 'Changelog' file in the package source).

Mao, J. and Ma, L. (2022), “Dirichlet-tree multinomial mixtures for clustering microbiome compositions,” *The annals of applied statistics*, 16, 1476.

Park, P. J. (2009), “ChIP-seq: advantages and challenges of a maturing technology,” *Nature reviews genetics*, 10, 669–680.

Pique-Regi, R., Degner, J. F., Pai, A. A., Gaffney, D. J., Gilad, Y., and Pritchard, J. K. (2011), “Accurate inference of transcription factor binding from DNA sequence and chromatin accessibility data,” *Genome research*, 21, 447–455.

Polson, N. G., Scott, J. G., and Windle, J. (2013), “Bayesian inference for logistic models using Pólya–Gamma latent variables,” *Journal of the American statistical Association*, 108, 1339–1349.

Rauluseviciute, I., Riudavets-Puig, R., Blanc-Mathieu, R., Castro-Mondragon, J. A., Ferenc, K., Kumar, V., Lemma, R. B., Lucas, J., Chèneby, J., Baranasic, D., et al. (2024), “JAS-PAR 2024: 20th anniversary of the open-access database of transcription factor binding profiles,” *Nucleic acids research*, 52, D174–D182.

Rodriguez, A., Dunson, D. B., and Gelfand, A. E. (2008), “The nested Dirichlet process,” *Journal of the American statistical Association*, 103, 1131–1154.

Scrucca, L., Fraley, C., Murphy, T. B., and Raftery, A. E. (2023), *Model-Based Clustering, Classification, and Density Estimation Using mclust in R*, Chapman and Hall/CRC.

Sethuraman, J. (1994), “A constructive definition of Dirichlet priors,” *Statistica sinica*, 639–650.

Sherwood, R. I., Hashimoto, T., O'donnell, C. W., Lewis, S., Barkal, A. A., Van Hoff, J. P., Karun, V., Jaakkola, T., and Gifford, D. K. (2014), "Discovery of directional and nondirectional pioneer transcription factors by modeling DNase profile magnitude and shape," *Nature biotechnology*, 32, 171–178.

Song, L. and Crawford, G. E. (2010), "DNase-seq: a high-resolution technique for mapping active gene regulatory elements across the genome from mammalian cells," *Cold Spring Harbor Protocols*, 2010, pdb-prot5384.

Teh, Y. W. (2006), "A hierarchical Bayesian language model based on Pitman-Yor processes," in *Proceedings of the 21st International Conference on Computational Linguistics and 44th Annual Meeting of the Association for Computational Linguistics*, pp. 985–992.

Teh, Y. W., Jordan, M. I., Beal, M. J., and Blei, D. M. (2006), "Hierarchical dirichlet processes," *Journal of the american statistical association*, 101, 1566–1581.

Wang, H. (2012), "Bayesian graphical lasso models and efficient posterior computation," *Bayesian Anal.*, 7, 867–886.

Supplementary Materials for “A tree-based kernel for densities and its applications in clustering DNase-seq profiles”

S1 Proof of Proposition 1

Proof. According to Theorem 3.16 and Theorem 3.19 in Ghosal and Van der Vaart (2017), we need to verify 2 conditions: (1) $\{V_{\epsilon 0}, \epsilon \in \mathcal{E}^K\}$ are all fully supported on $[0, 1]^{2K}$; (2) for arbitrary probability measure λ ,

$$\sup_{K \in \mathbb{N}} \max_{\epsilon \in \mathcal{E}^K} \frac{\mathbb{E} \left(\prod_{l=1}^K V_{\epsilon_1 \dots \epsilon_l}^2 \right)}{\lambda^2(A_{\epsilon_1 \dots \epsilon_l})} < \infty.$$

The first condition is easy to verify since $\psi_{\epsilon,0}$ follows multivariate normal and $V_{\epsilon 0} = \text{logit}^{-1}(\psi_{\epsilon,0})$. For condition (2), for K large enough, take λ to be the uniform measure and given that we have the first L -layer of splitting variables that follow a multivariate normal

distribution,

$$\frac{\mathbb{E} \left(\prod_{l=1}^K V_{\epsilon_1 \dots \epsilon_l}^2 \right)}{\lambda^2(A_{\epsilon_1 \dots \epsilon_l})} = \mathbb{E} \left(\prod_{l=1}^L (2V_{\epsilon_1 \dots \epsilon_l})^2 \right) \prod_{l=L+1}^K \mathbb{E} ((2V_{\epsilon_1 \dots \epsilon_l})^2)$$

Since L is a finite fixed layer, we can denote the first term $C_L = \mathbb{E} \left(\prod_{l=1}^L (2V_{\epsilon_1 \dots \epsilon_l})^2 \right)$, where C_L is finite that also depends on μ and Σ . In the remaining term, $\mathbb{E} \{(2V_{\epsilon_1 \dots \epsilon_l})^2\} = 4\text{Var}(V_{\epsilon_1 \dots \epsilon_l}) + 4\mathbb{E} \{V_{\epsilon_1 \dots \epsilon_l}\}^2$.

Because we assume that for independent ψ_ϵ , they follow independent normal distribution with mean μ_ϵ and variance σ_ϵ^2 , and $V_\epsilon = \text{logit}^{-1}(\psi_\epsilon) = \frac{1}{1+e^{-\psi_\epsilon}}$. Note that $h(x) = \frac{1}{1+e^{-x}}$ is a Lipschitz function with Lipschitz constant 1/4, i.e. $|h(x) - h(y)| \leq 1/4|x - y|$.

Hence given the assumption that $\sigma_\epsilon^2 \leq \gamma_l$,

$$\begin{aligned} \text{Var}(V_{\epsilon_1 \dots \epsilon_l}) &= \text{Var}(h(\psi_{\epsilon_1 \dots \epsilon_l})) \leq \mathbb{E} \{ [h(\psi_{\epsilon_1 \dots \epsilon_l}) - h(\mathbb{E}\psi_{\epsilon_1 \dots \epsilon_l})]^2 \} \\ &\leq \frac{1}{16} \mathbb{E} [\psi_{\epsilon_1 \dots \epsilon_l} - \mathbb{E}\psi_{\epsilon_1 \dots \epsilon_l}]^2 = \frac{1}{16} \text{Var}(\psi_{\epsilon_1 \dots \epsilon_l}) \\ &\leq \frac{1}{16} \gamma_l \leq \gamma_l. \end{aligned}$$

Similarly, given the assumption $|\mu_\epsilon| \leq \delta_l$, and note that $\sup_x |h'(x)| \leq 1/4$,

$$\begin{aligned} |\mathbb{E} \{V_{\epsilon_1 \dots \epsilon_l}\} - 1/2| &= |\mathbb{E} \{h(\psi_{\epsilon_1 \dots \epsilon_l})\} - \mathbb{E}(h(0))| \\ &\leq \frac{1}{4} |\mathbb{E}(\psi_{\epsilon_1 \dots \epsilon_l}) - 0| \leq \frac{1}{4} \delta_l \leq \delta_l \end{aligned}$$

With a similar argument as in Theorem 3.16 in Ghosal and Van der Vaart (2017),

$$\mathbb{E} \{(V_{\epsilon_1 \dots \epsilon_l})^2\} = \text{Var}(V_{\epsilon_1 \dots \epsilon_l}) + \mathbb{E} \{V_{\epsilon_1 \dots \epsilon_l}\}^2 \leq \gamma_l + (\delta_l + 1/2)^2 = (1 + 4\gamma_l + 4\delta_l^2 + 4\delta_l)/4$$

Then

$$\sup_{K \in \mathbb{N}} \max_{\epsilon \in \mathcal{E}^K} \frac{\mathbb{E} \left(\prod_{l=1}^K V_{\epsilon_1 \dots \epsilon_l}^2 \right)}{\lambda^2(A_{\epsilon_1 \dots \epsilon_l})} \leq C_L \prod_{l=L+1}^{\infty} (1 + 4\gamma_l + 4\delta_l^2 + 4\delta_l)$$

Now given that $\sum_l (\delta_l + \gamma_l) < \infty$, $\sum_l \gamma_l < \infty$ and $\sum_l \delta_l < \infty$, hence $\delta_l \rightarrow 0$ as $l \rightarrow \infty$, and when l is large enough, $\delta_l^2 < \delta_l$, hence $\sum_l \delta_l^2 < \infty$. Denote $a_l = 4\gamma_l + 4\delta_l^2 + 4\delta_l$, $\sum_l a_l < \infty$.

Note that when $x \geq 0$, $1 + x \leq e^x$. Hence $\prod_l (1 + a_l) \leq \prod_l e_l^a = e^{\sum_l a_l} < \infty$. Condition (2) is verified. □

S2 Posterior derivation for Gibbs sampling algorithm

Posterior of ψ_i and its hyperparameters

We vectorize all splitting variables ψ_i from top to bottom, from left to right. The tree vectorization code is implemented in `vectorize_tree` C++ function in our R package. Denote the vectorized splitting variable as ψ_i . Allow the first L splitting variables to be correlated. Denote I as the collection of independent splitting variables, and C as the collection of correlated splitting variables. $\psi_i = (\psi_{i,C}, \psi_{i,I})^T$ is assigned a multivariate normal prior with block-diagonal covariance matrix. For group $Z_i = k$, the prior for $\psi_{i,C}$ is normal with mean $\mu_{k,C}$ and precision matrix $\Lambda_{k,C}$. This precision matrix $\Lambda_{k,C}$ is updated using the GHS prior proposed by Li et al. (2019) and implemented in our Rcpp package. The prior for $\psi_{i,I}$ is normal with mean $\mu_{k,I}$ and variance $\sigma_{k,I}^2$.

We use the Pólya-gamma augmentation (Polson et al., 2013) approach to update ψ_i . For any given parent node A_ϵ and its left child node A_{ϵ_0} . Let $n_i(A_\epsilon)$ be the number of counts in node A_ϵ for subject i . Denote the auxiliary variable $\omega_i(A_\epsilon) \sim \text{PG}(n_i(A_\epsilon), \psi_{i,\epsilon_0})$. The posterior of $\psi_{i,C}$ given $Z_i = k$ follows

$$\begin{aligned} \psi_{i,C} | \dots &\sim N\left((\Lambda_k + \Omega_{i,C})^{-1}(\Lambda_k \mu_{k,C} + \kappa_{i,C}), (\Lambda_k + \Omega_{i,C})^{-1}\right) \\ \Omega_{i,C} &= \text{diag}\left\{\{\omega_i(A_\epsilon)\}_{\epsilon \leq L}\right\}, \quad \kappa_{i,C} = \left\{n_i(A_{\epsilon_0}) - \frac{n_i(A_\epsilon)}{2}\right\}_{\epsilon \leq L} \end{aligned}$$

Note that Λ_k is allowed to be dense, and we use Cholesky decomposition to speed up the inverse $(\Lambda_k + \Omega_{i,C})^{-1}$. The posterior for $\psi_{i,I}$ is similar if we replace Λ_k by $\text{diag}\{\sigma_{k,I}^{-2}\}$ ($\sigma_{k,I}$ is a vector that shrinks to 0 for deeper layers), $\mu_{k,C}$ by $\mu_{k,I}$, and the corresponding $\Omega_{i,I}$ and $\kappa_{i,I}$. We put hyper prior $N(0, \sigma_\mu^2)$ to each element in $\mu_{k,C}$ and $\mu_{k,I}$.

For the independent part, $\sigma_{k,I}^2$ is assigned inverse-gamma prior $\text{InvGamma}(\alpha_0, \beta_{0,I})$, where α_0 is a hyperparameter, and $\beta_{0,I}$ is a vector such that for ψ_{i,ϵ_j} where $\epsilon_j > L$, $\beta_{0,j} = 1/|\epsilon_j|$ where $|\epsilon_j|$ is the layer index for ϵ_j . The posterior of $\sigma_{k,I}^2 \sim \text{InvGamma}(\alpha_0 + n_k/2, \beta_{0,I} + S_j/2)$, where n_k is the number of elements in group k , $S_j = \sum_{i:Z_i=k} (\psi_{i,\epsilon_j} - \mu_{k,\epsilon_j})^2$.

Posterior of Z_i, π_k

The posterior of $Z_i = k$ is a discrete distribution on $k = 1, \dots, K$, where $P(Z_i = k | \dots) \propto \pi_k P(\psi | Z_i = k, \dots)$. The likelihood $P(\psi | Z_i = k, \dots)$ is the normal prior assigned to ψ in the previous session.

The mixing proportion π_k is assigned a stick-breaking prior GEM (α) (set to 1 in practice). The stick-breaking distribution can be updated through a series of beta random variables, $V_k \stackrel{\text{iid}}{\sim} \text{Beta}(1, \alpha)$, $\pi_1 = V_1$, $\pi_k = V_k \prod_{l < k} (1 - V_l)$. Let n_k be the number of subjects in group k . For $k = 1, \dots, K-1$, $V_k | Z, \alpha \sim \text{Beta}(1 + n_k, \alpha + \sum_{l=k+1}^K n_l)$. In practice, we use

the gamma distributions $G_{k,1} \sim \text{Gamma}(1 + n_k, 1)$ and $G_{k,2} \sim \text{Gamma}(\alpha + \sum_{l=k+1}^K n_l, 1)$ to compute $V_k = G_{k,1} / (G_{k,1} + G_{k,2})$.

S3 Additional Simulation Results

Due to the complexity of the cor-tree model, the mixture of multiple cor-tree can be challenging to converge to the global optimum without a reasonably good initial value, especially in the case of low-count samples. In the simulation and real data analysis, we use the PAM result as the initial value for the membership variable Z .

To validate the choice of using PAM as the initial values for Z in the real data analysis, we conduct a simulation study where the simulated data has the same row sum (total count per sample) range from 100 to 2156, the same $n = 570$ and $K = 221$ as the REST data. Note that the true signal patterns are the same as the simulation design in Figure 2b, where there are only 2 clusters. In Section 4, the row sums can range from 4×10^3 to 10^4 . Table S1 provides the results for two experiments, where the prespecified number of clusters can be 3 or 5.

Table S1: Clustering results based on 100 replications. Columns meaning from the 3rd column to the last one: mean, median, and standard deviation of ARI over 100 replications, number of times ARI=0 or 1 over 100 replications. Results that only include positive ARI cases are marked with *pos ARI*.

Experiment	Method	Mean_ARI	Median_ARI	SD_ARI	n_zero_ARI	n_one_ARI
nclus = 3	K-means	0.27	0.27	0.03	0	0
	PAM	0.30	0.31	0.07	0	0
	Ind-tree	0.41	0.40	0.18	0	0
	Cor-tree	<u>0.55</u>	0.84	0.47	42	7
	Cor-tree (pos ARI)	0.94	0.99	0.09	0	7
nclus = 5	K-means	0.16	0.13	0.05	0	0
	PAM	0.24	0.25	0.04	0	0
	Ind-tree	0.17	0.14	0.12	1	0
	Cor-tree	<u>0.50</u>	0.71	0.46	45	4
	Ind-tree (pos ARI)	0.17	0.14	0.12	0	0
	Cor-tree (pos ARI)	0.90	0.95	0.12	0	4

Based on Table S1, first, the overall performance of all methods deteriorates compared with Table 1 when there are sufficient counts per sample. This is particularly an issue for Cor-tree. Because the non-parametric tree model with covariance structure is complex enough as one component of the mixture model, when there is insufficient count data to explore such a complex structure, the cor-tree model tends to collapse into one big cluster for all samples. The mode collapsing ending with a single cluster leads to 42 cases where ARI=0 when the preset cluster number is 3, and 45 cases with ARI=0 with 5 preset clusters.

However, we also observe that in the case where Cor-tree can indeed identify more than 1 cluster, the clustering accuracy is very high in both experiments, with both mean and median ARI above 0.9. The results after removing the 0 ARI cases are marked with *pos ARI* in Table S1. This provides evidence that the real data analysis can choose PAM as the initial value for Z , and as long as the result in the real data does not have mode collapsing, the clusters are likely close to the truth, whereas competing methods such as k-means and PAM may have far worse results.

S4 Additional Real Data Results

This section provides additional real data analysis results.

Figure S1 provides the real data analysis results when K-means and PAM are also allowed to find at most 5 clusters. In this plot, there exists some small-sized clusters, such as group 5 in K-means and group 4 in PAM, that exhibit the bi-modal pattern and could be potential TFBS. However, the histogram plot indicates that k-means and PAM still fail to identify most of the TFBS, but group 5 in PAM is most likely a subgroup of the TFBS.

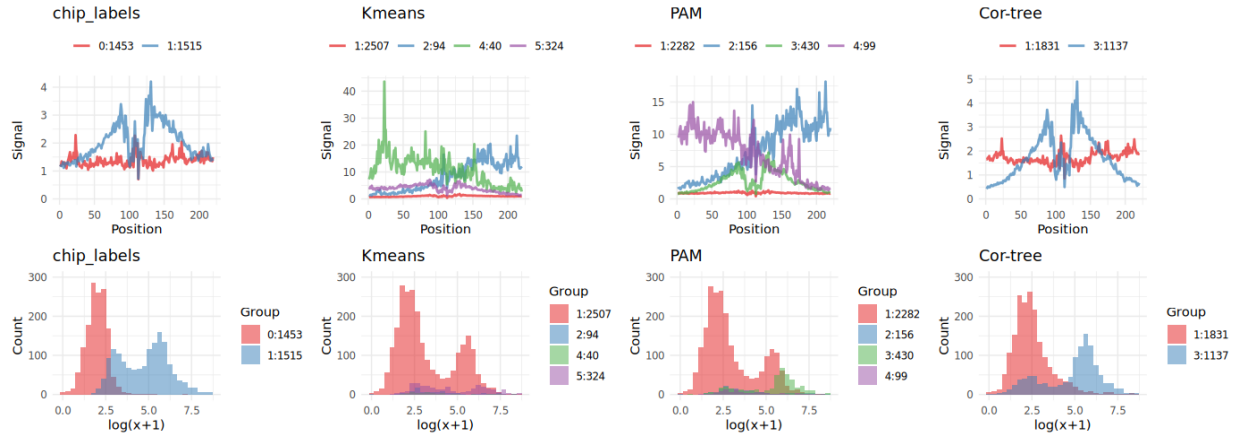


Figure S1: REST data clustering result when each method is allowed to have at most 5 clusters.

Similarly, Figure S2 shows the result when K-means and PAM are both allowed to have at most 5 clusters. Both PAM and K-means further split the binding group into smaller clusters, but they have similar geometric patterns. Cor-tree can automatically collapse into 2 clusters even though we set the total number of clusters to be 5.

Figure S3 shows the traceplots of 30 iterations of the 5-dimensional mixing weight π after burn-in for both REST and NRF1 data. The stable traceplot indicates good convergence of the mixing weight π .

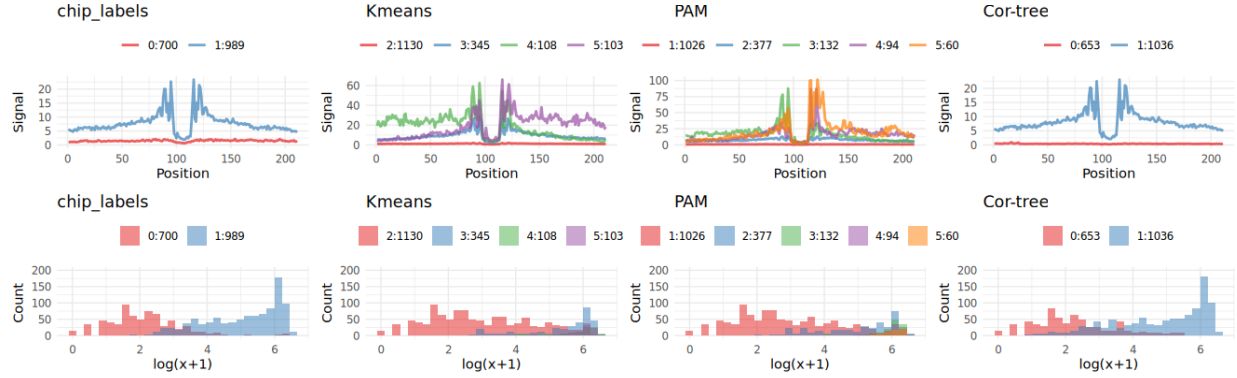


Figure S2: NRF1 data clustering result when each method is allowed to have at most 5 clusters.

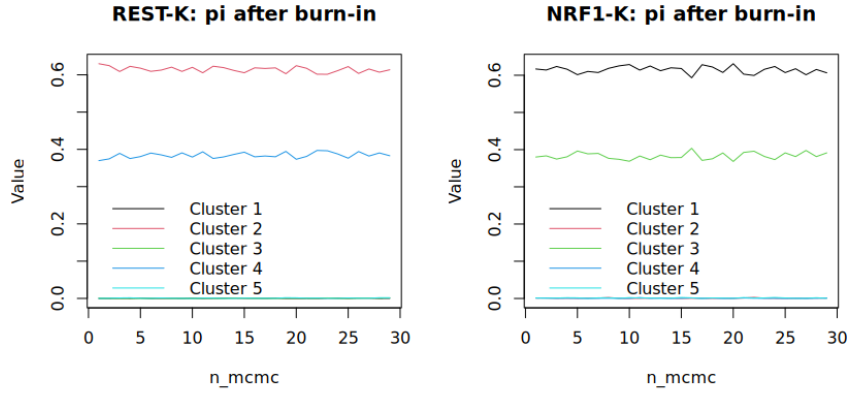


Figure S3: REST and NRF1 traceplot for the mixing weights π 30 iterations after burn-in.

We perform sensitivity analysis for the REST and NRF1 results reported in the main paper for the following 3 values: the number of clusters (denoted as K in the following plots), the hyperparameter α_0 in the prior $\sigma_{k,I}^2 \sim \text{InvGamma}(\alpha_0, \beta_{0,I})$ (denoted as c in the following plots), and the hyperparameter σ_μ^2 (denoted as sig2) in the hyper-prior $N(0, \sigma_\mu^2)$ for $\mu_{k,C}, \mu_{k,I}$. Table S2 shows the hyperparameter setting used in the main result. In the sensitivity analysis, we vary each hyperparameter and report the result in Figure S4. The result in Figure S4 indicates that the Cor-tree clustering result is generally robust to slight changes in these three hyperparameters. In NRF1 sensitivity results, when the number of clusters is set to 6, the non-binding group is further split into two subgroups, but the binding group is still consistent.

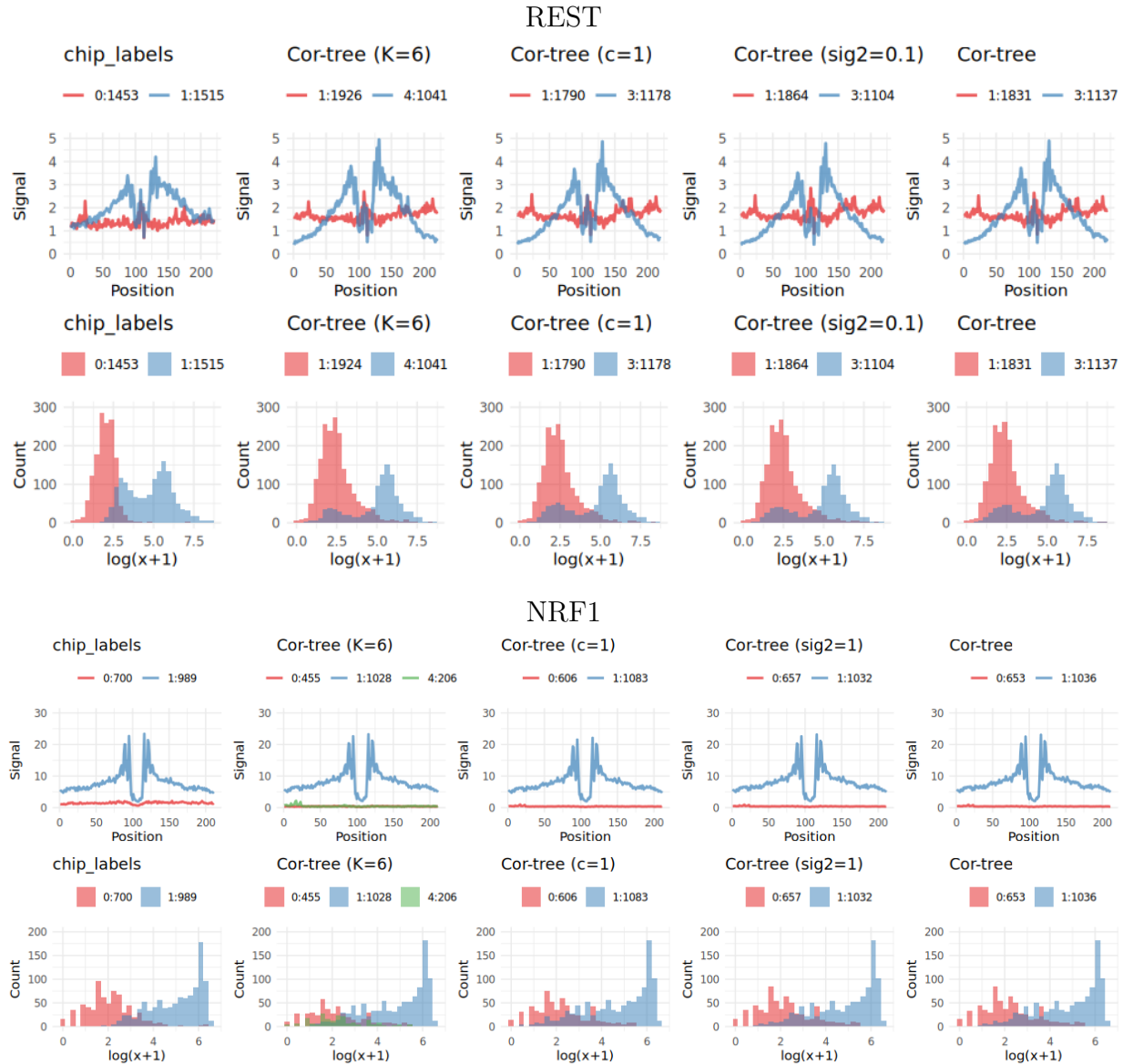


Figure S4: Sensitivity analysis results for REST and NRF1. Each column is one different hyperparameter compared with the main result setting in Table S2.

	K	c	sig2
REST	5	10	1
NRF1	5	10	0.1

Table S2: Hyperparameter setting for the main result.